Chapter 4
Enhancement of multiferroic and optical properties in $BiFeO_3$ due to different exchange interactions between transition and rare earth ions

4.1 INTRODUCTION

Multiferroic materials are of particular attention due to the co-existence of ferromagnetic (FM)/antiferromagnetic (AFM) and ferroelectric (FE) properties[5]. At present, multiferroic (MF) materials are the subject of demanding research since MF materials potentially offer a wide range of new applications in multiple-state memory devices such as the newly growing area of spintronics and new data-storage media [144]. In addition, according to recent studies of multiferroics, bismuth ferrite has narrow band gap characteristics that make it excellent for potential photovoltaic and photo-catalytic applications[145,146]. A semiconducting material's band gap energy is minimized by the addition of some dopants. It raises the number of electrons in the conduction band and eventually slows down the recombination, which boosts photocatalytic activity [147]. Bismuth ferrite is a remarkable visible-light sensitive photo-catalyst for water splitting and the decomposition of organic contaminants[148]. Only $BiFeO_3$ exhibits G-type canted antiferromagnetic ordering from all the known MF materials at the temperature, T_N = 643 K, and ferroelectric ordering at the temperature T_C = 1103 K[28]. Significantly, these ordering temperatures are much greater than the room temperature. At ambient temperature, polycrystalline $BiFeO_3$ (BFO) multiferroic has a rhombohedral crystal structure with the space group R3c. In BFO G- type AFM ordering with the spiral structure of spins with a period 620 ± 20 Å[149,150] counteract the material's macroscopic magnetization.

Before BFO-based devices can be made commercially feasible, several challenges must be overcome, including high dielectric loss, high leakage current density, secondary phase impurities, chemical fluctuations, inhomogeneous magnetic spin structure, and poor ME coupling [151]. Different approaches have been attempted to reduce leakage currents such as synthesis using various chemical routes, doping at the A and B-site of BFO, and growing high-quality single crystal and thin films[94,135,152–154]. We choose the ionic substitution

strategy over the others as it can suppress the spiral spin structure and enhance its magnetization. Chemical substitution at the Bi/Fe sites of BFO with appropriate ionic radius elements has been reported to produce a stable perovskite phase. A-site doping with rare-earth minerals such as La[32], Pr[155], Sm[156], Dy[157], Gd[158], Eu[37], Tb[34], and Ho[36] can significantly alter particle size, lattice structure, surface morphology, and the number of oxygen vacancies, improving the ferromagnetic and ferroelectric properties of BFO whereas the B-site doping with transition metal elements such as Mn[159], Ni[160], and Co[161] can reduce leakage current, improving electric polarization and magnetization in MF. Furthermore, by replacing Bi^{3+} and Fe^{3+} ions with (Sm, Ba, La, Gd, Y, Eu, Tb) and (Co, Ti, and Mn) respectively, the ferromagnetic characteristics of BFO can be improved[37,45,162–165].

With this background, we have chosen Tb and Mn doping at A and B sites respectively, which may enhance the ferroelectric and magnetic properties by eliminating leakage current or by inducing internal pressure (crystal structure change). Tb was chosen as a dopant for its significant-high magnetic moment (9.72 μB/at.), which will have the ability to improve the magnetic properties of the system. Terbium electro-negativity is comparable to that of Bi^{3+} (1.45 Å) ion, similarly, Tb ionic radius (1.25 Å) is also comparable for A site 12- fold coordinates system[82,166–168]. Moreover, the ferromagnetic coupling is also one of the main consequences of Tb doping which leads to structural change by releasing the latent magnetization that had been trapped inside the spin cycloid[151]. At the B site, the unfilled Mn^{3+} orbital and filled Fe^{3+} orbital are supposed to enhance the ferromagnetism according to the Goodenough-Kanamori rule [169]. Similar to other reported doped systems, e.g., $Bi_{1-x}Dy_xFeO_3$[170], we expect that there will be band reconstruction due to co-doping in the present system, which will improve the optical property. Moreover, the magnetic property of perovskite oxides is highly sensitive to doping on its site as a different dopant will change/deform its lattice structure [171]. Thus, it is expected that the co-doping will improve

the magnetic property in the present system. In this article, we focus primarily on optical, dielectric, and magnetic properties. Additionally, the significant absorption of UV light and rise in the intensity of absorbance in t visible area act as additional motivation for the synthesis of newer optical devices.

4.2 EXPERIMENTAL DETAILS

To synthesize $(Bi_{0.90}Tb_{0.1})(Fe_{0.90}Mn_{0.1})O_3$ (BTFMO91) samples, the traditional solid-state reaction pathway technique was followed using high-purity materials including Fe_2O_3, Bi_2O_3, Mn_2O_3, and Tb_4O_7. High-purity oxides were weighed carefully in stoichiometric ratio and an extra 5% of Bi_2O_3 was added because Bi has volatile nature at high temperatures then all oxides were grinded together for around 2-3 hours. Then calcined for about 3 hours at 810 ^oC and cooled down to room temperature. The calcined powder was then re-ground, pelletized (10 mm diameter at 5-ton pressure), sintered at 850 ^oC for 6 hours, cooled to room temperature slowly (50^oC each hour), and sintered for another 12 hours. All of the heat treatments were done at atmospheric pressure. The sample is structurally studied using an X-ray diffractometer with Rigaku Miniflex – II Cu Kα radiation (λ=1.5406 Å). The Fullprof suite software was used to refine the X-ray diffraction (XRD) data. To know the magnetic behavior of the system, magnetic measurements were performed with the magnetic Property Measurement System (SQUID-MPMS, Quantum Design, USA. A vibrating sample magnetometer (VSM) was used to study the sample's magnetic properties at a high temperature (300–650 K). A PD2 neutron powder diffractometer (λ=1.2443Å) located at the Dhruva reactor in the Atomic Research Centre in Mumbai, India has been used to measure neutron diffraction. We used an Omicron Multi-probe Surface Science System to confirm the oxidation states of the synthesized sample using X-ray photoemission spectroscopy (XPS) investigations. The average base pressure is set at $2.8x10^{-11}$ Torr throughout. The total energy resolution was 0.25eV, based on the

width of the Fermi edge. Using a JASCO -750 UV-Vis spectrophotometer, the UV-Vis absorption spectra of all the phosphors were recorded spanning the wavelength range of 200–860 nm. The FTIR spectra were captured using the JASCO FTIR 4600. An extremely sensitive Keysight E4980A Precision LCR meter with a He-cooled CCR (closed-cycle refrigerator) was used to measure the dielectric properties.

4.3 RESULTS AND DISCUSSION

4.3.1 ULTRAVIOLET - VISIBLE (UV-Vis) SPECTROSCOPY:

Ultraviolet-visible (UV-Vis) spectroscopy is a useful tool for determining the energy band gap of materials. The optical absorption capacity of materials in the visible and near-visible ranges is studied using UV- Vis spectroscopy at RT in the range of 200– 860 nm, as shown in Figure 1(a). Based on this absorption spectrum, BTFMO91 has a significant capability for absorbance in both the visible and UV regions. Additionally, for the direct band-gap semiconductor, the band gaps were calculated from the Tauc plot. The Kubelka–Munk function F(R) given by $F(R) = (1-R)^2/2R$, where R is the diffuse reflectance of the material. $(\boldsymbol{\alpha}h\boldsymbol{\nu})^2 = (h\boldsymbol{\nu} - E_g)$ where $\boldsymbol{\alpha}$ = F(R), $h\boldsymbol{\nu}$ (photon energy), the direct band gap values can be extrapolated from the graphs for $(hv)^2 \rightarrow 0$, as illustrated in the inset of Fig. 1 (a). The energy band gap (Eg) of BTFMO91 was calculated using Tauc's relation

$$\boldsymbol{\alpha h\nu} = A(\boldsymbol{h\nu} - \boldsymbol{E_g})^n \quad \textbf{(1)}$$

Where α is the absorption coefficient, h is the Planck constant, A is a constant, $\boldsymbol{\nu}$ is the photon's frequency, E_g is the band–gap, and n = 1/2; n value provides a detailed overview of the transition in a material. The Tauc plot shows that the BTFMO91 system has a band gap at energy E_g = 1.83 eV which is similar to as observed by Kumari et al., Zhong et al., Pattnaik et al. [172–174]. As M. Sakar et al. has discussed in their system that due to Dy doping, there is the formation of a new electronic state of Dy^{3+} underneath the pure BFO material.

Similarly in our system, we have doped Tb at the Bi site, thus there may be the formation of the new electronic state of Tb^{3+}, as a result, the band gap decreased in our system. Other than this the co-substitution generates the change in structure, and also in the Fe-O-Fe bond angle (shown in Table 1), any modification in the bond angle additionally impacts the band gap of BFO. The Fe-O-Fe exchange angle, consequently, affects the hybridization between Fe 3d and O 2p, as a result, the smaller energy band gap in this system [170]. In different forms of the material, such as bulk, nanomaterial, or single crystalline material, pure BFO has a band gap in the range from 2.1 eV to 2.7 eV, which is quite large compared to BTFMO91 system[175,176]. The narrower bandgap of BTFMO91 suggests that it might be used for photocatalysis with visible light (i.e wastewater treatment, degradation of the pollutants, solar cell devices), and it has a huge amount of potential for energy-related applications[38,146,147,174,177,178]. As UV- Vis spectrum is visible 400-700 nm is optimal, so the composite materials will be able to produce a greater number of e^{-}–h^{+} pairs.

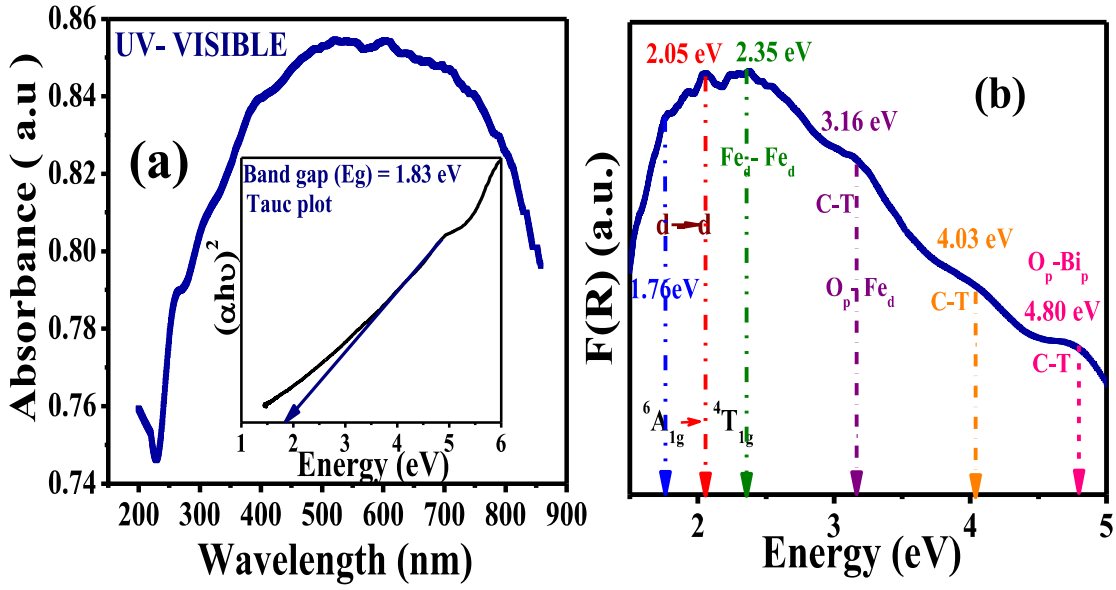

Figure 4.1: *(a) The UV-Visible absorption spectrum of $Bi_{0.9}Tb_{0.1}Fe_{0.9}Mn_{0.1}O_3$, inset of 1 (a) shows the Tauc plot. (b) Room temperature Diffuse Reflectance UV–VIS spectroscopy plots depicting the electronic transitions.*

Furthermore, the lower value of the band gap of the BTFMO91 system can also be

understood by reflectance measurement. T. D. Rao *et al.*, and T. Karthik *et al.*, explained the lower band gap value with the help of UV-Visible absorption spectra of BFO compounds at room temperature. They have shown the diffuse reflectance (R) spectrum using the Kubelka-Munk function F(R) and plotted it as a function of energy E (eV) [166]. However, we have also plotted and found a similar kind of F(R) *vs.* energy behavior as shown in Figure 1(b) [166,179]. Although BFO's cubic structure is deformed (rhombohedral), there seems to be a point group symmetry breaking to C_{3v} from O_h [180]. If the C_{3v} local symmetry of Fe^{3+} ions ($3d^5$ – High spin configuration; $t_{2g}^3 e_g^2$) is considered in BFO and the correlation group and subgroup analysis for the local symmetry breaking from O_h to C_{3v}, then there are up to six d–d transitions expected between 0 and 3 eV [181,182]. However, we have also found three excitations in our system between zero to 3 eV energy. Whereas, between 1.7 to 5 eV range spectrum of F(R) shows six absorption bands. There is an anomaly around 1.76 eV occurring because of the transition between $^6A_{1g} \rightarrow {}^4T_{1g}$ in BFO, which is caused by Fe^{3+} d–d crystal field excitations. Generally, these excitations are prohibited because they alter Fe^{3+} spin to S= 3/2 from S= 5/2. However, spin-orbit coupling relaxes the spin selection process and as a result, this type of transition may occur as explained by X. S. Xu et al. [183]. Similarly, the absorption significantly increases above 2.2 eV, with a broad shoulder centered at 2.35 eV (i.e Fe_1 3d –Fe_2 3d transition), and three prominent peaks near 3.16 eV, 4.03 eV, and 4.80 eV related to charge transfer (CT) excitations[180,181,183,184]. The Fe–O bond length, site symmetry, and Fe–O–Fe exchange interaction are all factors that influence the position of this d–d transition. However, upon closer inspection, the d-d and CT transition bands for BFO compounds appeared to have a little redshift [185]. The presence of a noticeable shift in these transition bands shows that the substitution of Tb and Mn in BFO enhances the internal chemical pressure that emerges as a result of changes in the FeO_6 local environment leads by the unit cell volume

contraction[115]. Thus, the present system's optical absorption demonstrated an optimal photo absorption property, implying that they could be used as more efficient photocatalysts.

4.3.2 FOURIER TRANSFORM INFRARED SPECTROSCOPY:

The composite BTFMO91 Fourier Transform Infrared Spectroscopy (FTIR) spectrum was measured in the wavenumber range of 400–2000 cm^{-1} at room temperature, as shown in Fig. 2. The prominent peaks are seen in spectra of a pristine BFO system with Tb and Mn co-doping at 403, 538, 848, 1068, 1390, 1463, and 1732 cm^{-1}.

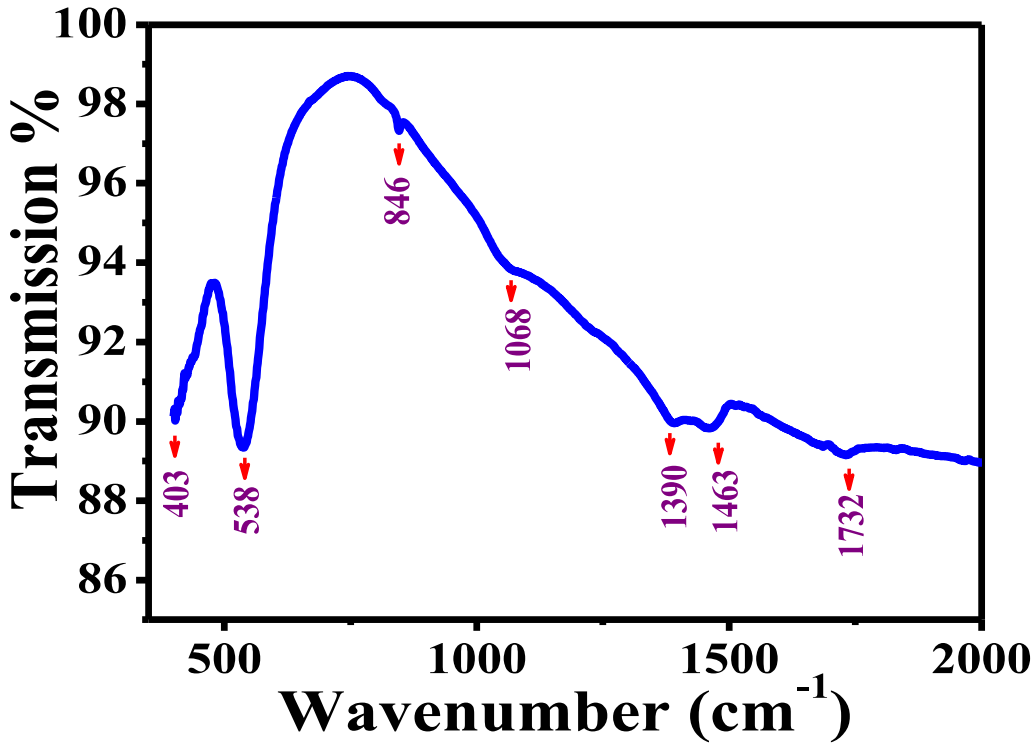

Figure 4.2: *FTIR spectra of $Bi_{0.9}Tb_{0.1}Fe_{0.9}Mn_{0.1}O_3$ system at room temperature.*

In the wavelength range of 400-550 cm^{-1}, fundamental absorptions are detected [186]. The overlap of the iron oxide and bismuth oxide vibration bands is the main reason behind the large absorption bands in our sample between 400-550 cm^{-1}. These absorption peaks are usually caused by O-Fe-O bending vibrations and Fe-O stretching of the FeO_6 group in a perovskite structure [147,187,188]. The vibration of the Bi–O bond is responsible for the band at

1068 cm^{-1} [189]. The band observed around 1390 cm^{-1} is attributed to the symmetry bending vibration of C-H or C-H_2 and the vibration of the carbonyl group [190,191]. The bands at 1500–1300 cm^{-1}, as well as peaks at 1120–1070 cm^{-1} and 850 cm^{-1}, indicate the presence of carbonate groups. There are a few more bands in the spectrum that can be distinguished in addition to these bands, such as the one at 1720 cm^{-1}, which is attributed to the bending vibrations of H_2O that are caused by the moisture absorbed by the system [192].

4.3.2 X-RAY DIFFRACTION STUDY:

For the BTFMO91 sample, R3c+$Pn2_1a$ (rhombohedral + orthorhombic) space groups are being used to refine the X-ray diffraction study (XRD) of prepared materials illustrated in Figure 3. The sample has been successfully fitted by both space groups confirming the absence of any impurity peak. In literature same system is prepared using sol-gel and solid-state methods in which they found the rhombohedral (R3c space group) phase with a secondary (impure) phase [115,193]. We have used the Fullprof program to perform Rietveld refinement crystallographic analysis for the XRD data. By doping (10% each at A and B sites) of Tb and Mn contents BTFMO91, we observed shifts in the peak positions as well as some new peaks, which also appeared and disappeared as compared to the pure BFO. Few previously reported works on A-site doped BFO also claimed to have a similar type of dual-phase space group [158,194]. For BTFMO91 composition it is observed that 24 % of the materials are orthorhombic $Pn2_1a$ phase and 76 % are rhombohedral R3c phase.

In our situation, the structural change may have occurred for a variety of reasons, including (a) in comparison to Fe^{3+} and Tb^{3+}, Mn^{3+}destabilizes R3c rhombohedral structure; (b) the lone pair of Bi^{3+} that seems to be stereochemically active is turned off when Tb^{3+} is substituted at the Bi-site since the ionic radii of Bi^{3+} and Tb^{3+} are 1.45 Å and 1.25 Å, respectively; (c) Chemical pressure of Tb^{3+} is substantially lower than that of Bi^{3+} since the larger ionic radii of Bi^{3+} compared to Tb^{3+} for high-spin eight-fold coordination, whereas

the ionic radii of Fe^{3+} and Mn^{3+} are the same (0.645 A) for high-spin six-fold coordination[34].

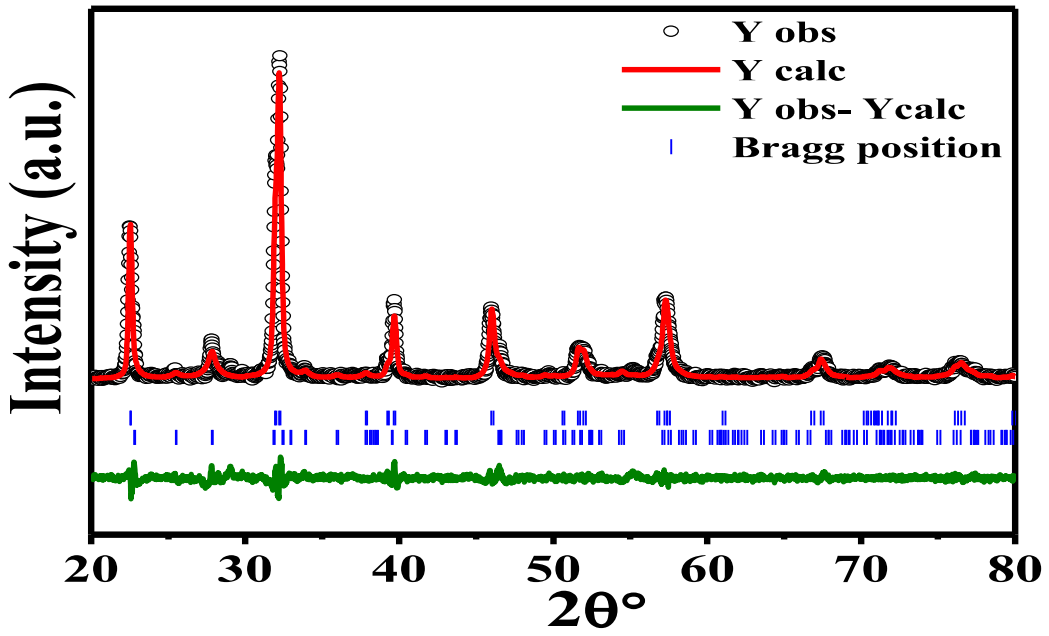

Figure 4.3: *Rietveld refinement of the X-ray diffraction data of* $Bi_{0.9}Tb_{0.1}Fe_{0.9}Mn_{0.1}O_3$ *system at room temperature.*

4.3.4 NEUTRON POWDER DIFFRACTION STUDY:

Figure 4 illustrates the temperature progression of the BTFMO91 neutron powder diffraction (NPD) patterns. A comparative data study in temperatures 6K – 300K is demonstrated in Fig. 4(a) in the confined 2Θ range of 4°−67°. The NPD data was effectively refined with the presence of both the nuclear (R3c and Pn21a) and magnetic (P-1) phases throughout all the measured temperatures. For the first R3c phase Bi/Tb, Fe/Mn, and oxygen atoms have the Wyckoff position of 6a, 6a, and 18b respectively. For the second Pn21a phase Bi/Tb, Fe/Mn, and oxygen atoms all have a 4a Wyckoff position[195]. XRD results also confirm the presence of two nuclear phases at RT. No trace of any phase impurity is found throughout the temperature range. It is observed that the magnetic

ordering makes a major contribution to the amplification of the peak intensity at ~ 13.74°, but the nuclear structure barely makes a minor or negligible contribution. Figure 4(b) shows the variation in the peak intensity of the super-lattice peak situated at ~ 13.74°in the temperature range 6 K- 300 K. The inset of figure 4(b) shows the corresponding variation of magnetic moment vs. temperature which shows a decrease at the moment as temperature increases.

In addition, it also indicates the non-zero value of the magnetic moment at RT of 0.5972 μ_B and the highest magnetic moment value at 6K (2.113 μ_B) suggesting the presence of weak ferromagnetism in the present system even at RT. Furthermore, figures 4(c) and 4(d) also illustrate the magnetic spin arrangement at both temperatures where the spin magnitude is larger at 6K compared to RT. The obtained spin structure at both temperatures shows a canted FM spin arrangement similar to some earlier work based on a double perovskite system [196]. Additionally, from the spin arrangement, we can infer that there are different types of interaction between all elements (the detailed discussion is present in the magnetic and XPS results section due to the mixed valence state observed for Tb, Fe, and Mn elements). In the system, these interactions additionally create competing FM and AFM interactions [195].

Both the crystal structure and the magnetic ordering of BFO are significantly altered by co-doping. The tolerance factor calculated from equation (2) for BTFMO91 is $r = 0.9279$. For an ideal perovskite structure, the r value should be unity. As doping is introduced, the r value decreases suggesting more ionic radius mismatching of dopants at the A and B sites of perovskite. As the r value is less than unity there is more change in the Fe-O-Fe bond angle and Fe-O bond length. Table 4.1 summarizes all the refined parameters which include the Wyckoff positions of the elements, occupancies, bond angle, bond lengths, etc.

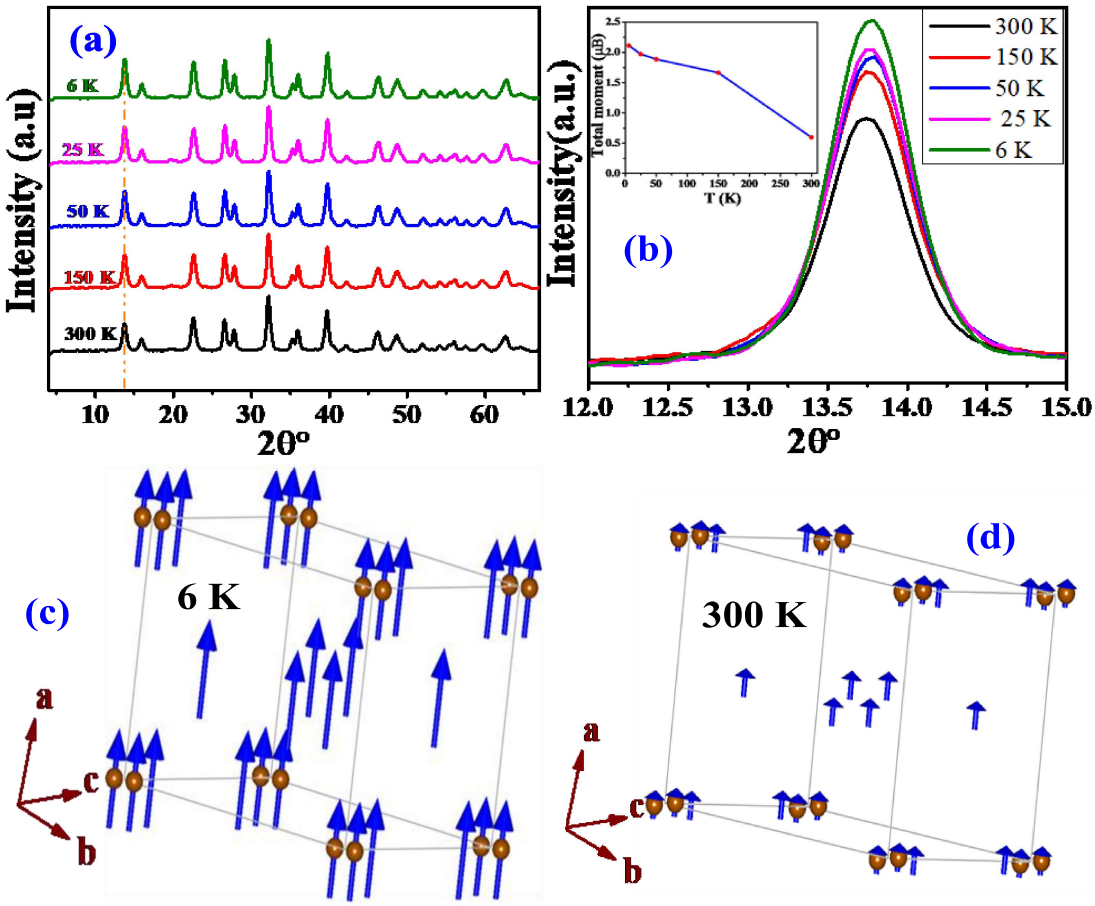

Figure 4.4: *(a)The Rietveld refined neutron powder diffraction pattern of* $Bi_{0.9}Tb_{0.1}Fe_{0.9}Mn_{0.1}O_3$ *at 300 K,150 K, 50 K, 25 K, and 6 K. (b) Variation of peak intensity with the temperature at 2Θ = 13.74 °, inset of 4(a) shows the temperature variation of the total magnetic moment. (c) And (d) Canted ferromagnetic type spin structure observed from Rietveld refinement of neutron powder diffraction at 300 K and 6 K respectively.*

Table 4.1: Structural parameters and crystallographic sites determined from Rietveld profile refinement of the NPD for $Bi_{0.9}Tb_{0.1}Fe_{0.9}Mn_{0.1}O_3$ at 6 K and 300 K. Space group: R3c and Pn21a.

NPD data recorded at	6K		300 K	
	R3c	$Pn2_1a$	R3c	$Pn2_1a$
For BTFMO91				
a (Å)	5.5606(1)	5.557(3)	5.5606(1)	5.567(3)
b (Å)	5.5606(1)	7.864(3)	5.5606(1)	7.878(3)
c (Å)	13.734(5)	5.568(4)	13.770(5)	5.573(4)
Bi/Tb (Site)	6a	4a	6a	4a
x	0.00000	0.00718	0.00000	0.00718

y	0.00000	0.35401	0.00000	0.35401
z	0.58885	0.73737	0.58885	0.73737
Fe/Mn (Site)	6a	4a	6a	4a
x	0.00000	-0.0278	0.00000	-0.0278
y	0.00000	-0.1224	0.00000	-0.1224
z	0.44136	0.12181	0.44136	0.12181
O(1) (Site)	18b	4a	18b	4a
x	0.19755	0.18952	0.19755	0.18952
y	1.41270	0.14031	1.41270	0.14031
z	0.33810	-0.0124	0.33810	-0.0124
O(2) (Site)		4a		4a
x		0.21634		0.21634
y		0.38064		0.38064
z		0.49389		0.49389
O(3) (Site)		4a		4a
x		0.29329		0.29329
y		0.37823		0.37823
z		-0.0190		-0.0190
Bond length				
Bi/Tb-O1	1.6687(3)	2.2493(10)	1.6707(3)	2.2526(10)
Bi/Tb-O2		1.7980(8)		1.8003(8)
Bi/Tb-O3		2.0986(9)		2.1016(9)
Fe/Mn-O1	2.4420(3)	2.2306(14)	2.4442(4)	2.2330(14)
Fe/Mn-O2		1.8718(9)		1.8749(9)
Fe/Mn-O3		2.3000(7)		2.3039(7)
Bond angle				
Mn/Fe-O-Fe/Mn (°)	163.238	156.64(9)	163.935	156.05(8)

4.3.5 X-RAY PHOTOELECTRON SPECTROSCOPY STUDY:

X-ray photoelectron spectroscopy (XPS) measurements were carried out at RT to study the oxidation (valence) states of the elements (Bi, Tb, Fe, Mn, and O) including the oxygen vacancy concentration in the BTFMO91 system. XPS is one of the most common surface-sensitive techniques for studying the valence states of any element in a material. The survey spectrum of the BTFMO91 system is shown in Figure 5(a), which reveals the presence of elements in stoichiometry. The Gaussian fitted spectra of Mn 2p, Fe 2p, and Bi 4f for the BTFMO91 system are shown in Fig 5(b)–5(d). Carbon (C) is present due to inadvertent molecules absorbed from the air near the surface. To eliminate the charging effect, the peak position of carbon C1s at 284.68 eV was used to calibrate the binding energy (BE) of all XPS spectra. XPS studies were conducted in BE range of 0–1400 eV to determine the

elemental ratio at the surface and the chemical composition. The XPSPEAK41 software was used to simulate and fit XPS data to determine the valence states. Bi core level splits into two main peaks $4f_{7/2}$ and $4f_{5/2}$ at BE 158.52 eV and 163.79 eV respectively for BTFMO91, demonstrating that Bi ions have the natural oxidation state of 3+ as shown in figure 5(b). The energy difference between the Bi $4f_{7/2}$ and Bi $4f_{5/2}$ peaks was 5.3 eV, which is consistent with previously published experimental and theoretical results [116,197].

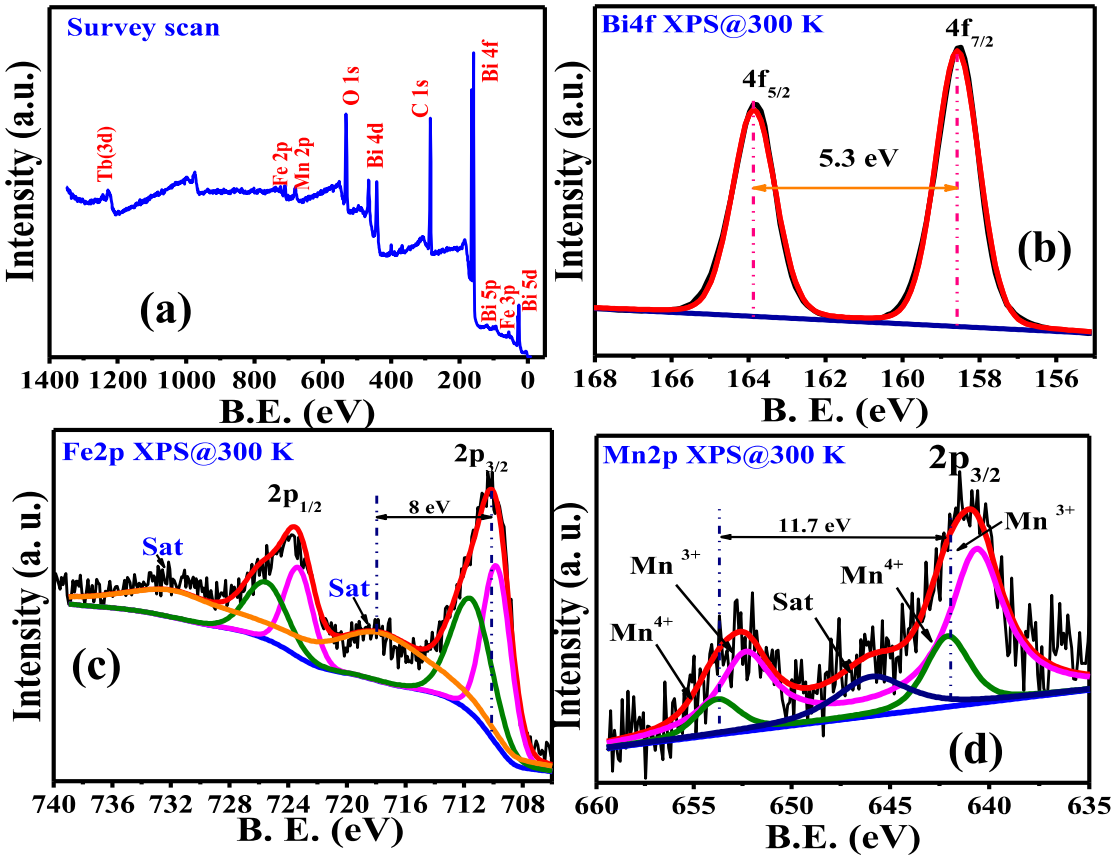

Figure 4.5: *The core level x-ray photoelectron spectroscopy (XPS) of $Bi_{0.9}Tb_{0.1}Fe_{0.9}Mn_{0.1}O_3$ system (a) survey scan (b) Bi 4f, (c) Fe 2p, and (d) Mn 2p respectively.*

The iron core level in the BTFMO91 system separates into two primary peaks $2p_{3/2}$ and $2p_{1/2}$ due to spin-orbit coupling, as shown in Figure 5 (c). We observed 6 peak deconvolution of Fe 2p at BE 709.76 eV, 711.48 eV, 718.09 eV, 723.3 eV, 725.48 eV, and 731.89 eV. The peak positions of Fe $2p_{3/2}$ and Fe $2p_{1/2}$ indicate both Fe^{3+} and Fe^{2+} states

coexist in the BTFMO91 system. The BE difference (spin-orbit splitting energy) between Fe $2p_{3/2}$ and Fe $2p_{1/2}$ peaks is 13.4 eV for the BTFMO91 system, which is again in good agreement with the standard value of 13.6 eV for the mixed oxidation state [122]. The Fe^{3+}: Fe^{2+} percentage ratio for the BTFMO91 system is approximately (70:30) as calculated from XPS peak fitting. The difference between the satellite peak and Fe $2p_{3/2}$ peak is 8 eV confirming that there is Fe^{3+} valency in plenty in our system[198]. For the BTFMO91 system, the Fe^{3+} percentage is more compared to Fe^{2+}, this might be associated with the reduction in oxygen vacancies which corresponds to the reduced leakage density (no secondary phase formation) in the system[199,200].

The two main peaks of Mn are at 652.94 eV and 641.05 eV with a doublet spacing of 11.7 eV for our system. The Mn2p XPS spectra in MnO_2 have a doublet separation of 11.8 eV, while Mn_2O_3 has a doublet separation of 11.6 eV (NIST)[195]. The observation of the intermediate value in our system suggests a mixed oxidation state of Mn ions. For further confirmation, we deconvoluted Mn2p XPS spectra as shown in Figure 5(d). The Mn core level splits into two main peaks $Mn2p_{3/2}$ and $Mn2p_{1/2}$ because of spin-orbit coupling. The Mn $2p_{3/2}$ peaks are at BE 640.61 eV and 642.08 eV and $Mn2p_{1/2}$ peaks are at BE 652.31 eV and 653.78 eV for the present system, whereas one satellite peak is also present at 645.91 eV for the BTFMO91 system [125,135,201]. Thus, there exists a mixed oxidation state of Mn (Mn^{3+} and Mn^{4+}) in our system.

4.3.6 MAGNETIC STUDY:

The magnetic characteristics of the BTFMO91 system were next investigated using zero-field cooling (ZFC) and field-cooling (FC) magnetization measurements across a broad temperature range of 4–300 K and field warming (FW) measurements in the range of 310 K - 650 K, with an applied field intensity of 100 Oe. The ZFC (black) and FC (red) graphs, and also the FW graph (inset), are illustrated in Fig. 6(a). From the field warming (FW)

measurement we observe the sudden change at the moment at 568 K[202] suggesting the magnetic transition temperature (T_N), whereas in pure BFO transition temperature is 643 K [203].

The magnetization field (M-H) graph of the BTFMO91 system at ambient temperature (300 K) and 5 K (low temperature) is illustrated in Figure 6(b). The magnetization at 50 kOe (at maximum field defined as M_H) observed from the M-H loop at 300 K and 5K are 1.23 emu/g and 9.94 emu/g respectively. As previously observed, the magnetization of the pure BFO changed linearly with the applied magnetic field, suggesting an antiferromagnetic nature, and M_H values were reported as 0.08 emu/g at 15 kOe, 0.35 emu/g at 55 kOe and ~0.25 emu/g 8 T at 300 K, in different studies[34,82,163,204]. However, in our system, the co-substitution introduced a typical non-linear magnetic hysteresis loop, suggesting a weak ferromagnetic-like ordering at both 5 K and RT. The weak ferromagnetic properties with the presence of antiferromagnetic characteristics of the system are shown by the unsaturated and a small loop at 300 K [inset figure 6(b)]. K.S. Kumar *et al.*, with a similar composition that is co-doping of Tb and Mn at both sites, shows weak ferromagnetic behavior which supports our results and the moment value (0.4 emu/g at 15 kOe and 0.51 emu/g at 20 kOe)[115,193]. Whereas, interestingly, the MH loops in this system measured at 5 K exhibits a non-linear response, suggesting the existence of modest ferromagnetism at low temperature, (inset figure 6(b)).

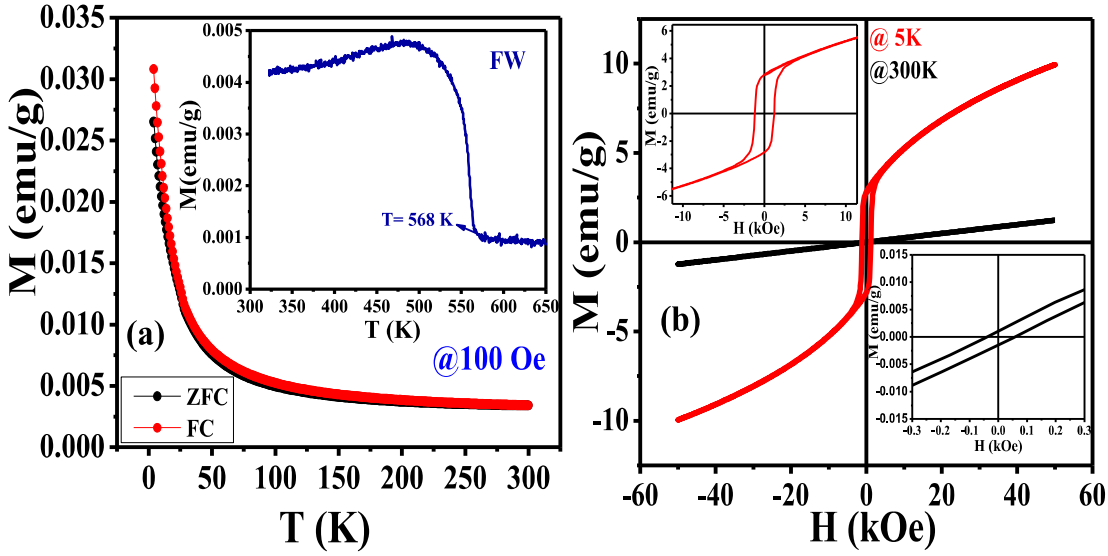

Figure 4.6: *(a) Moment vs. temperature curves measured for zero field cooling and field cooling conditions at 100 Oe in the temperature range 5 K – 300K. The inset demonstrates field warming data from 300K – 650 K temperature. (b) M (H) curves at 5 K and 300 K, inset of 4(b) show zoomed view at both temperatures of* $Bi_{0.9}Tb_{0.1}Fe_{0.9}Mn_{0.1}O_3$.

As an outcome, the overall M–H curve may be represented as a mixture of linear response (AFM) and nonlinear response (FM)[14,205]. The following could be the sources of the magnetization seen in the BTFMO91 composites: (1) As from the NPD study, the bond angle (i.e., from 180°) of the Fe-O-Fe distortion is arising due to the substitution of Tb and Mn at Bi and Fe sites respectively. Moreover, the Dzyaloshinskii–Moriya (D–M) interactions also explain that the degree of FeO_6 distortion depends on the degree of bulking in the system [206]. (2) The oxygen scarcity that results in the introduction of Fe^{2+} (from XPS) cations leads to the Fe^{3+}-O^{2}–Fe^{2+} interactions. The Fe^{3+}-O^{2}–Fe^{2+} also introduced canted spin construction and/or the reduction of spiral spin order as the crystalline size is reduced below 62 nm. Using the XRD data we fitted the Williamson-Hall plot (shown in the inset of Figure 4.3), and we found the crystalline size 60 nm [207]. Thus, these factors can contribute to the ferromagnetic behavior of the present system[208].

Further, the BFO matrix cycloidal spin structure also can be destroyed through this substitution, unleashing macroscopic magnetization. Similarly, the NPD study confirms

that the bond angle and bond length (i. e. shown in Table 1) changed and at RT spin is canted ferromagnetic type. XPS study shows that the different ions (Fe^{3+}, Fe^{2+}, Mn^{3+}, and Mn^{4+}) present in the system resulted in many competing AFM/FM interactions[195]. Moreover, according to the Goodenough–Kanamori[19] rule the empty Mn^{3+}/Mn^{4+} orbital and the full Fe^{3+}/ Fe^{2+} orbital should have a strong ferromagnetic interaction. There are different types of superexchange couplings according to the Goodenough-Kanamori rules combinations in these compounds [108,209].

(1) Mn^{3+}–O^{2-}–Mn^{3+} FM/AFM,

(2) Fe^{3+}–O^{2-}–Fe^{3+}, Mn^{4+}–O^{2-}–Mn^{4+} strong AFM,

(3) Fe^{3+}–O^{2-}–Mn^{3+} AFM/FM, (4) Fe^{2+}–O^{2-}–Mn^{4+} FM.

In addition, as nearest neighbors affect magnetism, the nearest neighbors of Tb^{3+} and Fe^{3+} have altered as Tb concentration has increased. This might also explain the reason behind larger magnetization in BFOs with greater doping [164]. As well as, the co-substitution suppresses the spin cycloid and releases the latent magnetization locked within the cycloid, which enhances the magnetization[210]. Furthermore, Tb^{3+} ions are strongly magnetic, enhancing magnetization and coercivity in Tb and Mn-modified materials while maintaining the spiral-modulated spin structure. Thus, the BTFMO91 system has competed for FM and AFM interaction even at room temperature.

4.3.7 DIELECTRIC STUDY:

Enhanced magnetic characteristics encouraged us to look into dielectric properties to discover more about insulating characteristics. Dielectric characteristics are influenced by various factors like doping, temperature, applied electric field, and structural defects. Figure 7 illustrates the dispersive type behavior of dielectric loss and relative dielectric permittivity (ε′) with frequency and temperature variation. The dielectric permittivity for

our BTFMO91 system progressively reduces with an increase in frequency (Fig. 7a) and becomes relatively constant above 100 kHz. The dielectric permittivity dispersion is linked with four distinct polarization mechanisms, each of which dominates at different frequencies. Dipolar and interfacial or space-charge polarization plays a key influence on the dielectric properties of BFO materials at lower frequencies, but electronic and ionic polarization plays a huge impact at higher frequencies [112,211]. The polarization of a sample is connected directly to its dielectric constant, and the separation of space charges is directly related to its polarization at low frequency. When an electric field is applied, the inclination of dipoles aligns themselves along the field direction resulting in dipolar polarisation, whereas the buildup of charges at the electrode interface or the inter-phase interface in material results in space charge or interfacial polarization. This can explain why the space charges can follow the frequency of the applied electric field at very low frequencies, but cannot follow the quickly changing applied field (oscillation) at high frequencies, as a result, the dielectric constant value reduces.

Electronic polarization is caused by the displacement of the electron cloud concerning the atom's nucleus when an electric field is applied, whereas ionic polarization is caused by the increase in the interionic distance between the positive and negative ions that are linked together by ionic bonds. It is anticipated that the main contributors to the dispersion of dielectric polarization will only be the dipolar and interfacial processes [212]. Furthermore, as has been observed in our XPS study, Fe^{3+}: Fe^{2+} percentage ratio for the BTFMO91 system is approximately (70:30), showing that the Fe^{3+} percentage is more compared to Fe^{2+}. Thus, the reason behind the finding of significant large dielectric dispersion in BTFMO91 might be explained by an electronic exchange, such as $Fe^{2+} \leftrightarrow Fe^{3+}$, originating from the Tb and Mn doping owing to the localized electron displacement in the direction of the applied electric field[212]. A similar phenomenon was reported by Lin et al., in RLS-BiFeO3

ceramics, where they explain that a relatively high resistivity was observed due to the low Fe^{2+} concentration, which reveals inherent dielectric characteristics[213].

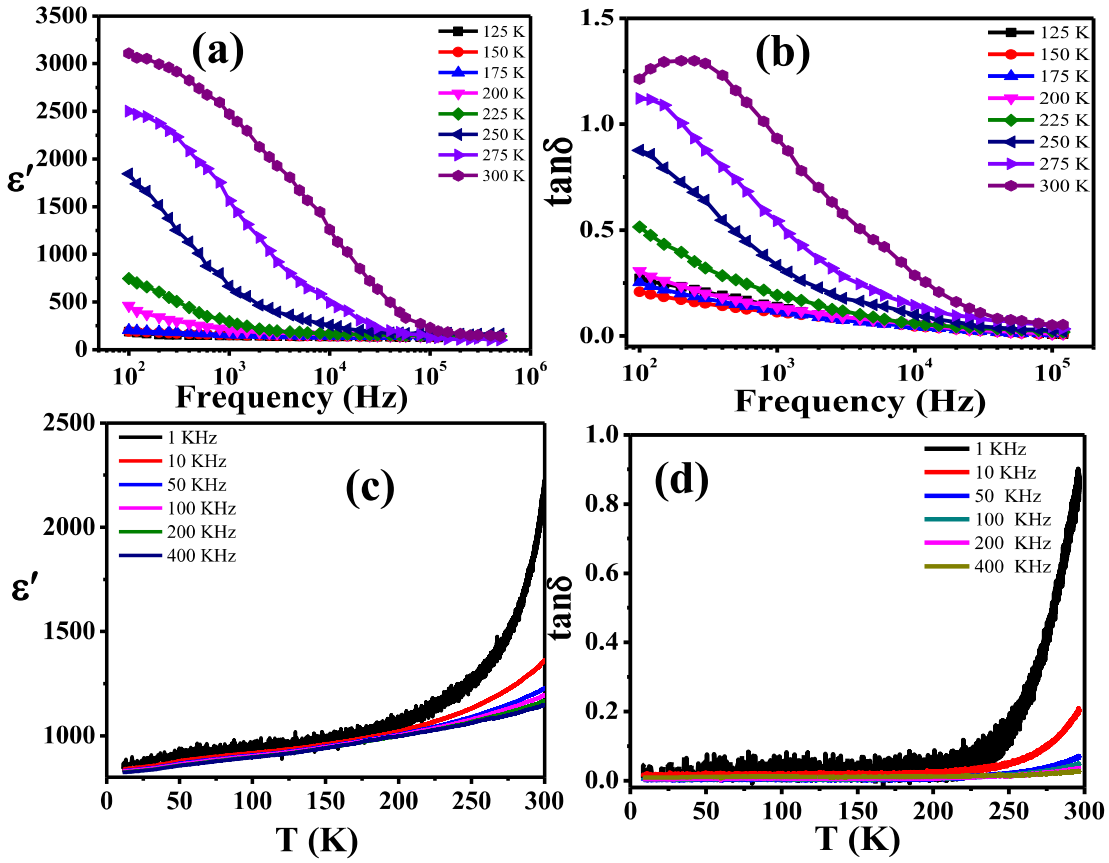

Figure 4.7: *Variation of (a) dielectric constant, and (b) dielectric loss with frequency at different temperatures. Variation of (c) dielectric constant, and (d) dielectric loss with the temperature at different frequencies of* $Bi_{0.9}Tb_{0.1}Fe_{0.9}Mn_{0.1}O_3$.

The Dielectric constant and dielectric loss value is calculated at different temperature ranges (125 K – 300 K) with frequency variation and we obtained the highest value at RT is ~ 3100, which is high compared to pure BFO. The dielectric loss (tanδ) explains the polarization lagging to the applied electric field as shown in the inset of Figure 7(a), which is following a similar trend as dielectric permittivity. The dielectric loss of the doped BFO is found to drop with an increase in frequency and its value is almost constant at higher frequencies. The lower dielectric loss value for this particular composition could be ascribed to a reduction in the impurity phase. Moreover, co-doping in the BFO system by

lower ionic radii element Tb at A site gives rise to the smaller grain size that increases the grain boundaries. Figures 7(b) and inset 7(b) depict the relative dielectric permittivity (ε′) and dielectric loss (tanδ) vs. temperature variation of the BTFMO91 system at different frequencies. Since dipoles freeze at low temperatures below ~ 200 K (100 Hz), the ε′–T curve reveals typically non-dispersive intrinsic polarization and a low value of ε′ at low temperatures below 200 K. ε′–T curve shows thermally active behavior as illustrated in figure 7(b); step type curve and as the frequency increase step shift toward higher temperature. The dielectric constant of $Bi_{0.90}Tb_{0.1}Fe_{0.90}Mn_{0.1}O_3$ as a function of temperature increases at higher temperatures (200-300 K) at different frequencies [214,215].

The literature shows that the BFO-based system has a significantly high leakage current problem which restricts this system's use for application purposes [115,216]. This leakage problem has been observed to be greatly decreased by doping of rare earth elements at A and B and in the structural study there is no impurity peak found in our system so our system can use as the application propose. We calculated the ε′ value ~3100 and the loss value is 1.5 at 100 Hz frequency. Due to their low value of dielectric loss BFO-based materials can be used for a variety of applications. However, the dielectric constant value ranges from 15 to 600, and the dielectric loss value is quite high for the pure BFO at room temperatures [111,112,204,211,212,217,218]. A previously published on $Bi_{0.90}Tb_{0.1}Fe_{0.90}Mn_{0.1}O_3$ compositions by K. Saravana Kumar *et al.*, with rhombohedral space groups, showed a lower value of the dielectric constant (260 at room temperature) [115,193].

4.4 CONCLUSION

In summary, we have synthesized a pure $Bi_{0.90}Tb_{0.1}Fe_{0.90}Mn_{0.1}O_3$ system by using the conventional solid-state method. A thorough analysis of the structural, magnetic, electrical, and optical properties was performed. The XRD data performed structural analysis using

Rietveld refinement, which identified a mixed orthorhombic and rhombohedral crystal structure with the space group Pn21a and R3c respectively. Neutron powder diffraction data refined with nuclear and magnetic phases at different temperatures which support the XRD data, low value of magnetic moment at room temperature gives information about the weak ferromagnetic property. From NPD we observe larger distortion in Fe-O-Fe bond length and bond angles. We found weak ferromagnetic behavior at room temperature as measured by magnetic (M-H curve). Whereas, in the magnetization measurement, we found that the Neel temperature of our system is 568 K. XPS measurement revealed a mixed valence state of Fe (Fe^{2+}, Fe^{3+}) and Mn (Mn^{3+}, Mn^{4+}) which further leads to different types of interaction resulting in weak ferromagnetic type behavior. Moreover, the dielectric constant increment and loss value decrease compared to the pure BFO system suggesting an enhancement in the dielectric property. The UV-visible absorption spectra exhibited a significant reduction of the band gap. The decreased band gap energy values found could signify that our system can be used as a photoactive agent.